Air-stable Membrane-free Magnesium Redox Flow Batteries
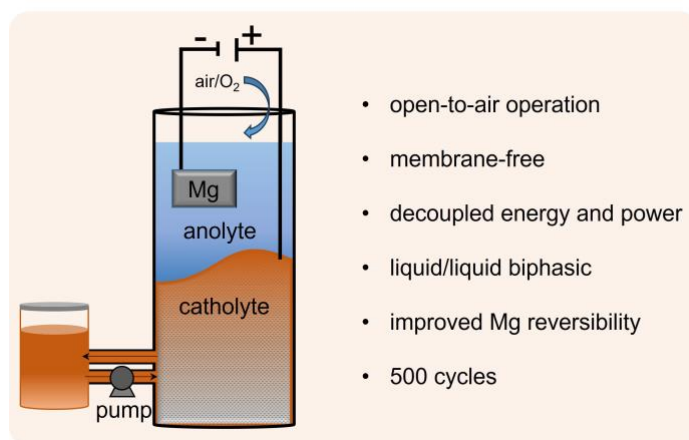
Rajeev K. Gautam[1], Jack J. McGrath[1], Xiao Wang[1], Jianbing "Jimmy" Jiang[1]*

[1]Department of Chemistry, University of Cincinnati, P.O. Box 210172, Cincinnati, Ohio 45221,

United States

*Corresponding author: Email: jianbing.jiang@uc.edu

Table of Content

- open-to-air operation
- membrane-free
- decoupled energy and power
- liquid/liquid biphasic
- improved Mg reversibility
- 500 cycles

Biphasic membrane-free Mg metal redox flow battery demonstrates high voltage and extended cycling life.

Abstract

Membrane-free biphasic self-stratified batteries (MBSBs), utilizing aqueous/nonaqueous electrolyte systems, have garnered significant attention for their flexible manufacturing and cost-effectiveness. In this study, we present an ultrastable high-voltage Mg MBSB based on an aqueous/nonaqueous electrolyte system. The engineered aqueous electrolyte has a wide electrochemical stability window of 3.24 V. The Mg metal anode features an Mg^{2+}-conductive protective coating. Two metal-free redox compounds, 2,2,6,6-tetramethyl piperidinyl oxy (**TEMPO**) and N-propyl phenothiazine (**C3-PTZ**), in dichloromethane serve as the catholyte. The Mg||**TEMPO** and Mg||**C3-PTZ** MBSBs exhibited high cell voltages of 2.07 and 2.12 V, respectively, and were studied under static, stirred, and flow conditions. The Mg MBSB was initially evaluated at different cathode concentrations (0.1, 0.3, and 0.5 M) under static conditions. Notably, Mg||**TEMPO** (0.5 M) and Mg||**C3-PTZ** (0.5 M) static batteries maintained exceptional performance over 500 cycles at 8 mA/cm², with capacity retention rates of 97.84% and 98.87%, Coulombic efficiencies of 99.17% and 99.12%, and capacity utilization of 70.2% and 71.3%, respectively. Under stirred and flow conditions, the Mg||**TEMPO** (0.5 M) and Mg||**C3-PTZ** (0.5 M) batteries cycled 500 times at 12 mA/cm², showing capacity retention rates of 99.82% and 99.88% (stirred), 93.58% and 92.16% (flow), respectively. The Mg||**TEMPO** (0.5 M) and Mg||**C3-PTZ** (0.5 M) batteries under flow conditions demonstrated power densities of 195 and 191 mW/cm², respectively, surpassing those of 139 and 144 mW/cm² under static conditions. These cost-effective Mg MBSBs offer remarkable performance, advancing Mg chemistry applications in organic flow batteries.

Keywords: Magnesium electrolyte; biphasic; membrane-free; self-stratified; redox flow battery

Introduction

The global pursuit of efficient and sustainable energy storage solutions has driven significant advancements in battery technology[1]. With the ever-increasing demand for renewable energy sources, there is a pressing need for robust energy storage technologies that can buffer intermittent energy production and provide reliable power supply[2,3]. Li-ion batteries have emerged as a dominant technology for various applications[4]. However, Li-ion batteries still encounter several formidable limitations, including limited material resources, high cost, and safety concerns[4,5]. These unresolved problems prompt the development of new types of batteries that could offer high energy density and better sustainability compared to Li-ion batteries. The potential alternatives to Li-ion batteries lie in utilizing other metals including alkaline earth metals (Mg^{2+}, Ca^{2+}), alkali metals (Na^+, K^+), group IIIA metals (Al^{3+}), and transition metals (Zn^{2+})[6]. Among the emerging alternatives, the Mg-ion battery has received significant attention due to the abundance of Mg, the high theoretical volumetric capacity of Mg compared to Li (3833 vs. 2046 mAh/cm^3), low cost, and environmental friendliness[7,8]. In addition, Mg metal demonstrates reduced dendrite formation during battery cycling, surpassing that of both Li and Zn, due to its low diffusion barrier and unique planar hexagonal growth during electrochemical deposition[8]. Hence, Mg-ion batteries hold the promise as a viable and sustainable energy storage technology, capable of meeting the escalating energy demands while mitigating environmental impacts.

Recent advancements in Mg-ion batteries have been primarily centered on solid-state rechargeable batteries[7,9]. Despite the significant progress made to advance the performance of Mg-ion solid-state batteries, the development of Mg-based flow batteries is still in the early stage. Only a few recent studies have been demonstrated by Qin et al.[10] and He et al.[11] using polymer and polysulfide as catholytes, respectively. Unlike solid-state rechargeable batteries, Mg flow batteries

3

offer independent scaling of energy and power, as well as compatibility to pair with diverse catholytes[12]. However, the implementation of Mg-based flow batteries faces significant obstacles, including (1) the limited availability and high costs of ion-exchange membranes in both aqueous and nonaqueous electrolyte systems[13,14], and (2) the requirement for electrolyte systems with highly reversible Mg chemistry[15,16]. The first issue can be addressed by utilizing membrane-free biphasic self-stratified batteries (MBSBs). Different configurations of MBSBs have been designed, and various redox chemistries have been explored by others[17-24] and our group[25-28]. An optimal biphasic system would include an anolyte with a highly reversible Mg anode and minimal solubility of cathode materials. Simultaneously, the catholyte should demonstrate high solubility and electrochemical stability for the redox-active cathode. In general, liquid/liquid biphasic systems are divided into three categories based on the solvents used for the anolyte and catholyte, including aqueous/aqueous[17,29], aqueous/nonaqueous[21-23,25], and nonaqueous/nonaqueous[24,26,28]. Before selecting a specific biphasic system to design a Mg MBSB system, it is imperative to thoroughly understand the electrochemical behavior of Mg metal within a particular type of electrolyte. The reversible chemistry of the Mg metal anode has been studied in both aqueous and nonaqueous electrolyte systems. Notable nonaqueous electrolyte systems explored for the Mg metal anode include Grignard reagents/tetrahydrofuran (THF)[30] or dimethyl ether (DME)[31], magnesium organoborate electrolyte, magnesium aluminum chloride complexes[32-34], Mg hexamethyldisilazane (Mg-HMDS)[35,36], and magnesium bis(trifluoromethanesulfonimide) $(Mg(TFSI)_2)$[37] (Figure 1). While some of these systems effectively prevent passivation film growth or facilitate reversible Mg stripping/plating, the organic solvents often exhibit electrochemical oxidative instability and poor conductivity[38]. In addition, the use of highly volatile ethereal solvents and metal complexes may raise safety and cost concerns[39]. Ionic liquids present a

4

promising alternative with their high electrochemical stability, low flammability, and high ionic conductivity[40,41]; however, the use of ionic liquid as a neat electrolyte solvent could be considerably expensive[42,43].
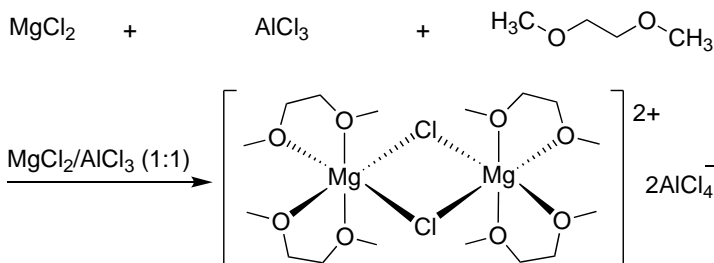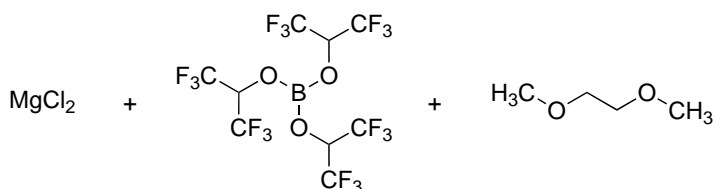
Grignard reagent
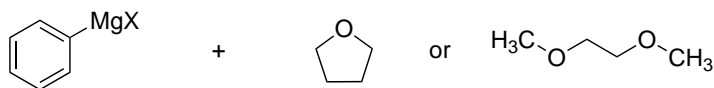
Mg/HDMS system
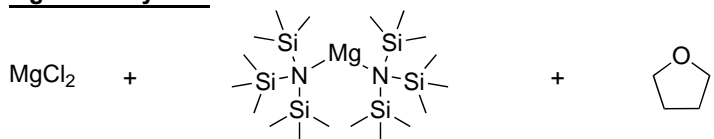
Mg/AlCl$_3$ complex

Mg/organoborate electrolyte system

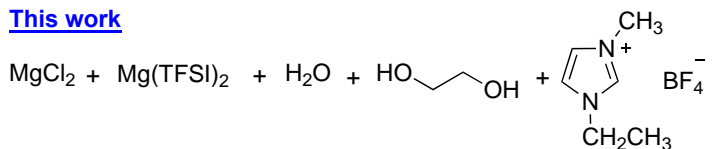**Mg(TFSI)$_2$ system**

This work

Figure 1. Electrolyte system. Reported electrolyte system for Mg ion batteries.

5

In contrast to nonaqueous systems, aqueous solvents offer the advantages of high ionic conductivity, low cost, safer operation, and environmental friendliness. However, aqueous electrolytes present two significant challenges when applied in Mg-ion batteries. Firstly, the tendency of Mg metal to form surface passivation layers comprised of magnesium oxide (MgO) and magnesium hydroxide (Mg(OH)$_2$) when exposed to water is a major hurdle[8]. Secondly, the narrow electrochemical stability window (ESW) of water (1.23 V) imposes constraints on achieving high cell voltage[44]. To address these challenges, extensive research efforts have been explored towards developing stable high-voltage aqueous electrolytes for Mg-ion batteries[8,45,46]. Notably, one promising approach involves the use of high-concentration Mg salts, such as magnesium chloride (MgCl$_2$) or Mg(TFSI)$_2$[8,45], aiming to reduce free water content, thus mitigating Mg surface passivation[8,45]. Another approach involves the use of solvent additives to enhance the ESW of aqueous electrolytes[46]. These strategies facilitate the direct utilization of Mg metal in aqueous electrolytes, thereby improving the kinetics of Mg-ion batteries.

In addition, the immiscibility of water with various nonaqueous solvents, whether in their neat form or through a salt-out strategy, facilitates the quick formation of stable aqueous/nonaqueous biphasic self-stratified systems. These systems are well-suited for the development of liquid/liquid membrane-free RFBs. In this study, we present the development of a membrane-free biphasic system based on aqueous/nonaqueous electrolytes (Supplementary Figure 1). The aqueous electrolyte, strategically modified with solvent additives including ethylene glycol (EG) and ionic liquid (IL), was paired with Mg metal serving as the anolyte. Meanwhile, the (dichloromethane (CH$_2$Cl$_2$)) electrolyte with organic redox compounds 2,2,6,6-tetramethyl piperidinyl oxy (**TEMPO**) and *N*-propyl phenothiazine (**C3-PTZ**) served as the catholyte. The developed anolyte was positioned on top of the catholyte, forming Mg||**TEMPO** and Mg||**C3-PTZ**

6

MBSBs with operational voltages of 2.07 V and 2.12 V, respectively. To prevent Mg metal passivation and enhance its reversible chemistry within the developed aqueous anolyte, we designed Mg metal with an effective Mg^{2+}-conductive polymer coating. Subsequently, the developed Mg||**TEMPO** and Mg||**C3-PTZ** MBSBs were evaluated for long-term charge/discharge under static, stirred, and flowing catholyte conditions. The newly developed cost-effective Mg MBSBs exhibit remarkable performance, thus paving the way for innovative applications in Mg chemistry within organic flow batteries.

Result and Discussions

Designing of electrolyte systems

To fabricate the biphasic system, water was utilized as the anolyte solvent. However, the narrow ESW restricts the development of batteries with a cell voltage greater than 1.7 V[45,47]. Therefore, widening the ESW of the aqueous electrolyte system is crucial to enable the use in Mg-based systems. Various strategies, including the use of water-in-salt and solvent additives, are widely explored for different battery applications[8,44-47]. In the water-in-salt strategy, higher concentrations of electrolyte salts are introduced into aqueous electrolytes to extend their ESW limit. The choice of salt is crucially important. The selected salts should exhibit high solubility in water and be electrochemically compatible with the redox material. Therefore, for the design of an aqueous anolyte for the Mg MBSB system, two Mg-based salts, $MgCl_2$ and $Mg(TFSI)_2$, were specifically selected due to the extensive studies in Mg-ion battery research[8,31,48]. The water/$MgCl_2$ (1 M) electrolyte system demonstrated an ESW of around 1.53 V (Figure 2). To further increase the ESW, different concentrations (0.2 M and 1 M) of $Mg(TFSI)_2$ salts were added to the water/$MgCl_2$ (1 M) electrolyte. The addition of both concentrations of $Mg(TFSI)_2$ salt broadened the ESW of the water/$MgCl_2$ (1 M) electrolyte. Notably, the water/$MgCl_2$ electrolyte with 1 M $Mg(TFSI)_2$

7

exhibited a slightly higher ESW compared to that of 0.2 M Mg(TFSI)$_2$. However, the use of a higher concentration of Mg(TFSI)$_2$ salt may increase the overall cost of the battery system. Therefore, a lower concentration of Mg(TFSI)$_2$ (0.2 M) in the water/MgCl$_2$ (1 M) electrolyte was selected for further electrochemical improvement.
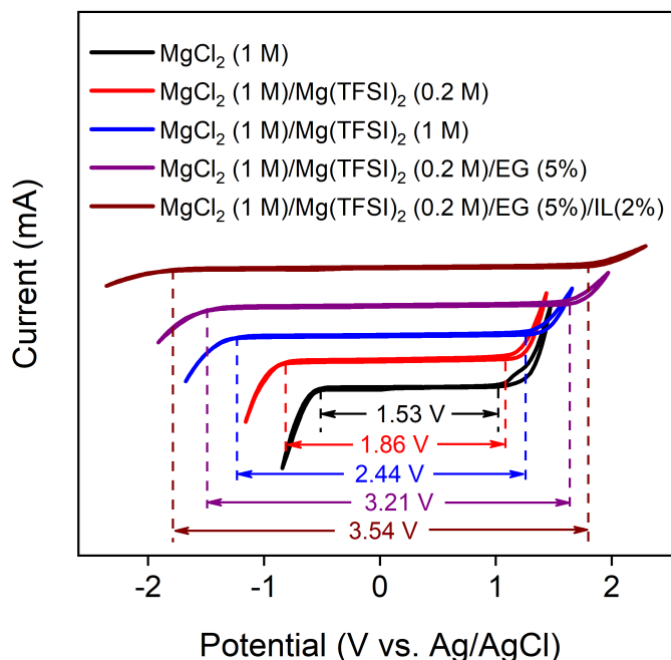

Figure 2. Electrochemical performance of developed electrolyte system. Electrochemical stability window of water with different concentrations of Mg salt and solvent additives.

The use of solvent additives is another strategy widely explored for enhancing the ESW of electrolytes[44]. Solvents with wide ESW and superior solvation compatibility are suitable candidates as solvent additives. Solvents such as ionic liquids (IL)[49], poly(ethylene) glycol (PEG)[50], and ethylene glycol (EG)[51] have previously been explored as promising solvent additives for expanding the ESW of aqueous electrolytes. Therefore, EG along with IL (1-ethyl-3-methylimidazolium tetrafluoroborate) were selected as solvent additives for aqueous electrolytes. The ability of EG to create stable complexes with magnesium ions[52], coupled with a wider ESW and high chemical stability of IL (Supplementary Figure 2), potentially contributes to a broader ESW for the aqueous electrolyte. The combination of EG and IL presents an optimal electrolyte

composition that can further extend the ESW of the developed aqueous electrolyte (Figure 2). Hence, EG (5%) and IL (2%) were added to the developed electrolyte system, resulting in the formation of water/$MgCl_2$ (1 M)/$Mg(TFSI)_2$ (0.2 M)/EG (5%)/ IL (2%) electrolyte with an electrochemical window of 3.53 V (Figure 2). The electrolyte salt potassium hexafluorophosphate (KPF_6) (0.25 M) was also added to the developed aqueous electrolyte to provide PF_6^- as an exchange charge carrier in the biphasic system. This finalized aqueous electrolyte system, water/$MgCl_2$ (1 M)/$Mg(TFSI)_2$ (0.2 M)/KPF_6 (0.25 M)/EG (5%)/ IL (2%), named WEIL, was employed consistently throughout all subsequent studies.

On the other hand, CH_2Cl_2 was selected as a cathode solvent for various reasons. First, the high solubilizing ability of CH_2Cl_2 allows the screen of a wide range of redox-active compounds. Second, the immiscibility of CH_2Cl_2 with water facilitates the formation of self-stratified biphasic systems. Third, the density of CH_2Cl_2 is higher than water, keeping the CH_2Cl_2 electrolyte at the bottom layer of the biphasic system to avoid direct air exposure of the catholyte. The use of CH_2Cl_2 as a catholyte solvent has been successfully demonstrated in our previous study[25]. Tetrabutylammonium hexafluorophosphate ($TBAPF_6$) (1.5 M) in CH_2Cl_2 was used as the electrolyte salt, which facilitates provided PF_6^- as an exchange charge carrier in the biphasic system.

Design of Mg metal anode with Mg^{2+} conductive polymer interface

The reversible Mg chemistry is crucial for the high and efficient performance of the Mg RFB system. In the developed electrolyte system, the use of solvent additives facilitates higher Mg reversible performance (Supplementary Figure 3). However, the Mg metal is still exposed to water molecules, exhibiting a high tendency to form a surface passivation layer. To mitigate this issue of passivation layer formation, high concentrations of salt in water have been explored to decrease

9

water content and prevent the passivation of the Mg metal anode[8]. Another strategy involves the application of polymer coatings, which are effective in protecting lithium and zinc metal anodes from dendrite formation[53,54]. The polymer coating establishes an ion-conducting interface between the electrolyte and the metal, effectively suppressing dendrite growth by preventing direct contact between the metal and the electrolyte. Motivated by this approach, we developed a modified Mg metal anode featuring a protective polymer layer capable of facilitating Mg^{2+} conduction from the electrolyte to the electrode surface. This strategy avoids direct contact of the Mg anode with water molecules, thereby significantly mitigating Mg surface passivation.

To prepare the surface-modified Mg metal anode, poly(vinylidene fluoride-co-hexafluoropropylene) (PVDF-HFP), $Mg(TFSI)_2$, and $Mg(OTf)_2$ salt were magnetically stirred in *N,N*-dimethylformamide for 24 hours in a 2:1:1 mass ratio to generate a clear polymer solution. The polymer solution was then coated onto the Mg metal surface following a dip coating process. After each coating, the polymer on the Mg metal surface was thermally polymerized before applying the next coat. A total of eight coatings were performed. Two additional Mg samples, PVDF-HFP/$Mg(TFSI)_2$ (2:1 mass ratio) and PVDF-HFP/$Mg(OTf)_2$ (2:1 mass ratio) were also prepared using the same method for control experiments. All processes were conducted in an argon-filled glovebox (moisture level < 1.0 ppm). A schematic of the preparation of the modified Mg metal anode is shown in Figure 3A. The surface morphology of the bare Mg metal anode and polymer-coated Mg metal anode are displayed in Figures 3B and 3C, respectively, suggesting that the polymer coating was uniform on the Mg metal surface.
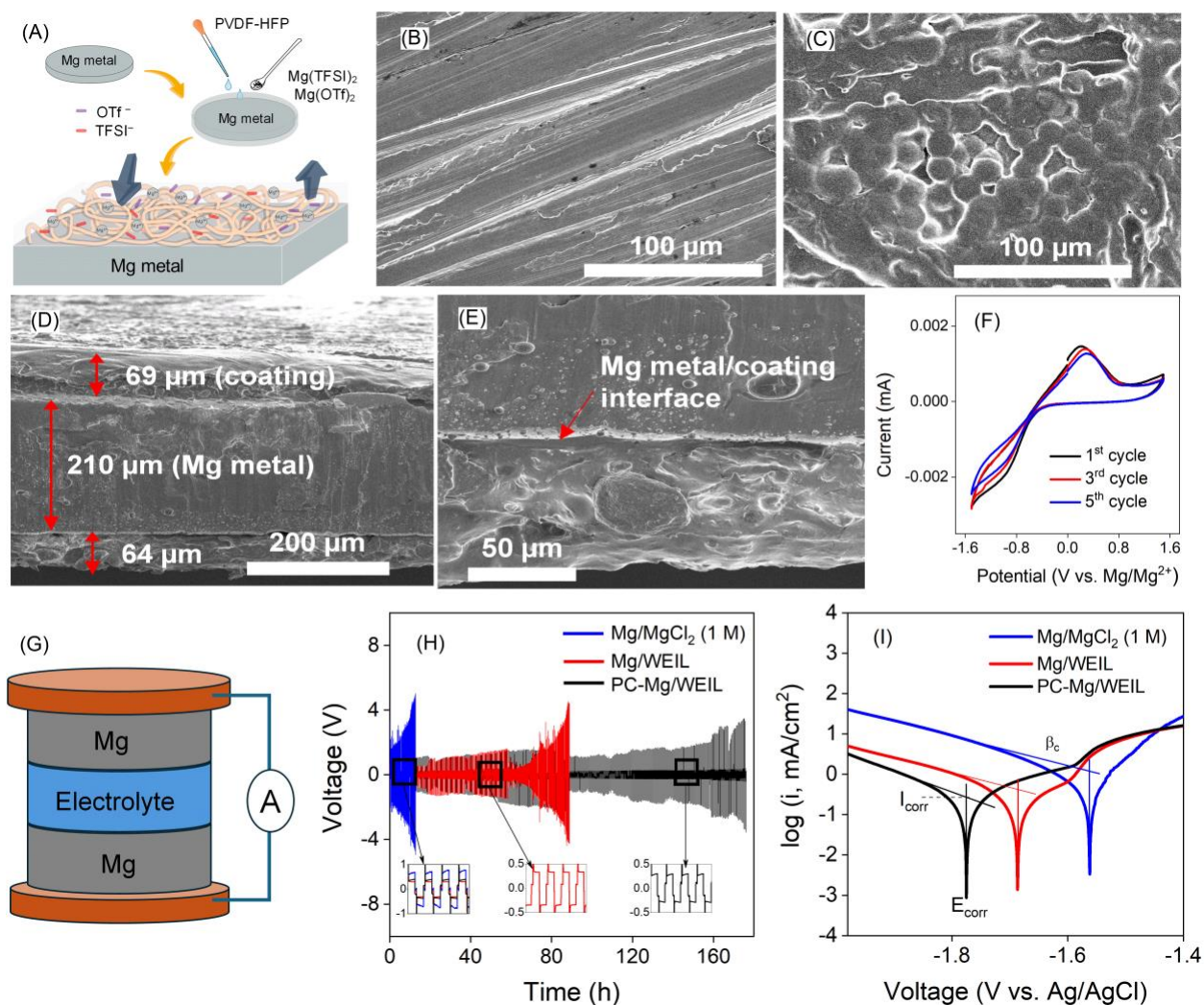
10

Figure 3. Polymer-coated Mg metal anode. (A) Schematic showing the microstructure of surface-modified Mg metal anode. (B) Surface morphology of bare Mg metal anode. (C) Surface morphology of surface modified Mg metal anode. (D) Surface morphology showing thickness of Mg metal anode and polymer coating. (E) Magnified surface morphology showing metal/coating interface. (F) Electrochemical reversibility of PVDF-HFP/Mg(TFSI)$_2$/Mg(OTf)$_2$ modified Mg metal anode in the developed aqueous electrolyte. (G) Schematic of Mg||Mg symmetrical cell. (H) Cycling stability of bare Mg||Mg symmetrical cell in 1 M MgCl$_2$ electrolyte, bare Mg||Mg symmetrical cell in WEIL electrolyte, and PC-Mg||PC-Mg symmetrical cell in WEIL electrolyte.

The metal anode was found to have a uniform coating of Mg^{2+} conductive polymer with an average thickness of approximately 65 µm (Figures 3D and 3E). Moreover, the energy dispersive X-ray (EDX) mapping analysis (Supplementary Figure 4) reveals the salt in the polymer coating was uniformly distributed. Electrochemical analysis reveals that Mg metal anode modified

11

with simply PVDF-HFP/Mg(OTf)$_2$ (Supplementary Figure 5) or PVDF-HFP/Mg(TFSI)$_2$ (Supplementary Figure 6) exhibit inferior Mg reversibility in comparison to that with PVDF-HFP/Mg(TFSI)$_2$/Mg(OTf)$_2$ (Figure 3F). The improved Mg reversible chemistry of PVDF-HFP/Mg(TFSI)$_2$/Mg(OTf)$_2$ modified Mg metal anode is attributed to better oxidative and high ion mobility behavior of Mg(OTf)$_2$ and Mg(TFSI)$_2$ salt, in combination[55-57]. Therefore, the PVDF-HFP/Mg(TFSI)$_2$/Mg(OTf)$_2$ modified Mg metal anode, named as PC-Mg, was used in all consecutive studies. Overall, the polymer-coated Mg metal anode, with an efficient Mg^{2+} conductive interface, minimizes direct contact between Mg and the electrolyte. This protects Mg from passivation by avoiding electrolyte reduction on the Mg surface, thus offering high Mg reversibility.

To assess the performance improvements provided by the WEIL and conducting polymer coating on the Mg metal anode (PC-Mg), we examined the cycling stability of Mg||Mg and PC-Mg||PC-Mg symmetrical cells (Figure 3G). The Mg||Mg symmetrical cell with a 1 M MgCl$_2$ electrolyte exhibited significant polarization after 22 hours of cycling (Figure 3H), indicating that the Mg stripping/plating process in 1 M MgCl$_2$ is unsustainable due to severe surface corrosion induced by severe hydrogen evolution reactions (HER). In contrast, the modified electrolyte system significantly enhanced Mg stability for 82 hours compared to the 1 M MgCl$_2$ electrolyte system. However, the modified electrolyte system (WEIL) cannot thoroughly prevent the Mg surface oxidation. Hence, further improvements are essential to enhance the Mg stability. The cycling stability of surface-modified PC-Mg||PC-Mg in the WEIL electrolyte displayed stable cycling behavior for 180 hours. The Mg^{2+} polymer conducting layer in PC-Mg metal significantly reduces surface corrosion by preventing direct contact with water molecules on the PC-Mg surface, thereby providing stable stripping/plating behavior. To gain further insight, corrosion experiments

12

were conducted (Figure 3I). It was observed that the PC-Mg/WEIL electrolyte reduced the corrosion current (i_{corr}) from 1.58 to 0.45 mA compared to the Mg/MgCl$_2$ (1 M) electrolyte, indicating a slower corrosion rate due to surface oxidation of the PC-Mg metal anode. Moreover, the β_c, which indicates the strength of HER[8], was reduced for the PC-Mg/WEIL system (297 mV/dec) compared to that of the bare Mg/MgCl$_2$ (373 mV/dec) metal anode. Hence, the PC-Mg/WEIL system significantly suppresses both surface corrosion and HER.

Selection of redox-active cathode materials

The rationale selection of redox-active cathode materials for the developed biphasic system is of utmost importance. To minimize crossover, a cathode material should exhibit high solubility in the catholyte solvent and minimal solubility in the anolyte. To identify catholyte materials meeting the solubility criteria, 11 redox-active compounds, including derivatives of phenothiazine (**C3-PTZ**), cyclopropenium (**CP**), 2,2,6,6-tetramethylpiperidin-1-yl)oxyl (**TEMPO**), and tetrathiafulvalene (**PEG3-TTF**) were tested for their solubilities in both phases of the biphasic system (Supplementary Table 2). Among the 11 compounds, **TEMPO** and **C3-PTZ** (Figure 4A) exhibited excellent solubility in the CH$_2$Cl$_2$ electrolyte and negligible solubility in the anolyte. Consequently, **TEMPO** and **C3-PTZ** were used as the cathode materials for subsequent electrochemical and battery cycling studies.

Electrochemical characterization

Cyclic voltammetry (CV) analysis was employed to investigate the electrochemical properties of cathode materials (Figure 4A) in CH$_2$Cl$_2$/TBAPF$_6$ (0.1 M) electrolytes. Both **TEMPO** and **C3-PTZ** displayed reversible redox couples at 0.34 V and 0.36 V vs. Ag/Ag$^+$ with a peak separation of 71 mV and 76 mV, respectively, at a scan rate of 50 mV/s (Figures 4B and 4C), indicating a one-electron redox process as per the Nernst equation.[58] In addition, CV measurements were

13

conducted at various rates ranging from 50–200 mV/s (Figures 4B and 4C) to study the electrochemical kinetics of the catholyte compounds. The ratios of the cathodic peak current (i_{pc}) and anodic peak current (i_{pa}) of **TEMPO** and **C3-PTZ** are close to 1 at the investigated scan rates (50–200 mV/s) (Supplementary Figures 7A and 7B), suggesting excellent electrochemical reversibility in the CH_2Cl_2 electrolyte. Moreover, the anodic and cathodic currents exhibited a linear relationship with the square root of the scan rate ($v^{1/2}$) for both **TEMPO** and **C3-PTZ** (Supplementary Figures 8A and 8B), indicating that the redox process is diffusion-controlled[58]. In addition to their remarkable electrochemical reversibility, both **TEMPO** and **C3-PTZ** display high electrochemical stability in the catholyte based on repeated CV scans (Figures 4D and 4E).
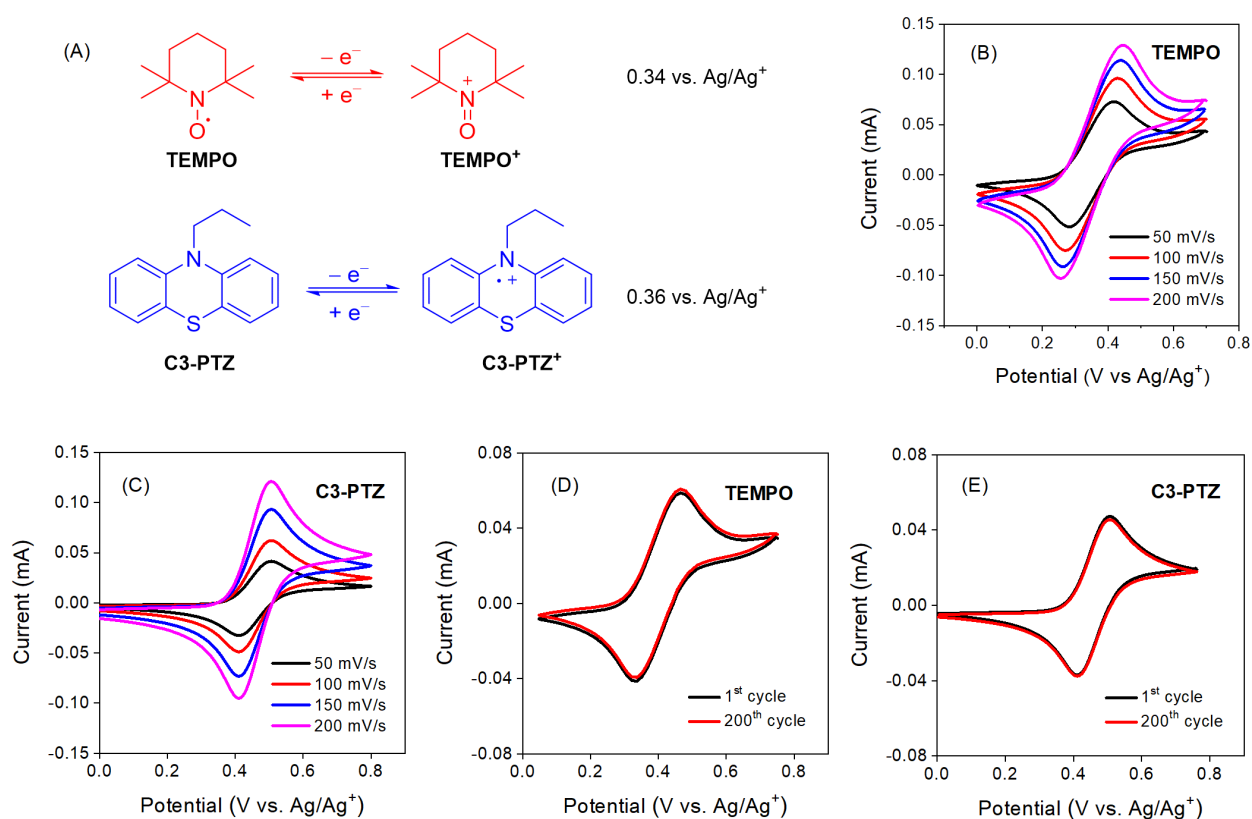

Figure 4. Electrochemical properties of redox-active cathode materials. (A) Chemical structures and redox voltages of **TEMPO** and **C3-PTZ**. Cyclic voltammograms of (B) **TEMPO** and (C) **C3-PTZ** at varied scan rates from 50 to 200 mV/s in CH_2Cl_2/TBAPF$_6$ (0.1 M). Cyclic voltammetry cycling stability of (D) **TEMPO** and (E) **C3-PTZ** for 200 cycles.

14

The diffusion coefficient of redox-active cathode materials dictates ion movement during charge and discharge, impacting overall electrochemical performance; therefore, characterizing the coefficient is essential for optimizing battery design and enhancing energy storage capabilities. Thus, the electrochemical kinetics of the catholyte molecules were studied by linear sweep voltammetry (LSV) with a rotating disk electrode (RDE) (Figure 5). The rotation rates (ω) were varied from 100 to 1600 rpm, which revealed distinct plateaus in the mass-transport-controlled limiting currents (i) (Figures 5A and 5B). The Koutecký–Lévich curves (Figures 5C and 5D) represent linear correlations between the limiting currents (i) and the square root of the rotation rate ($\omega^{1/2}$), for both **TEMPO** and **C3-PTZ** to measure the diffusion coefficient. From the slopes of the fitted linear Lévich plots (Figures 5C and 5D), the diffusion coefficients (D) for **TEMPO** and **C3-PTZ** were determined to be 4.78×10^{-6} and 4.86×10^{-6} cm^2 s^{-1}, respectively. The electrochemical kinetic rate constants of the charge-transfer reactions of cathodic redox materials were obtained using the Koutecky−Lévich equation (Eq. S2) (Figure 5E and 5F). The linear correlations between i^{-1} and $\omega^{-1/2}$ for **TEMPO** and **C3-PTZ** at different overpotentials (η = 10 to 100 mV) were used to estimate the i_k values. These i_k values were then plotted against the overpotential in Figures 5G and 5H. The kinetic rate constants (k_0) of **TEMPO** and **C3-PTZ** were calculated as 3.23×10^{-3} and 3.21×10^{-3} cm s^{-1}, respectively, using Eq. S2. Remarkably, the diffusion coefficients and rate constants of the catholyte materials are comparable to those of redox-active organic materials commonly used in aqueous flow batteries.[33]
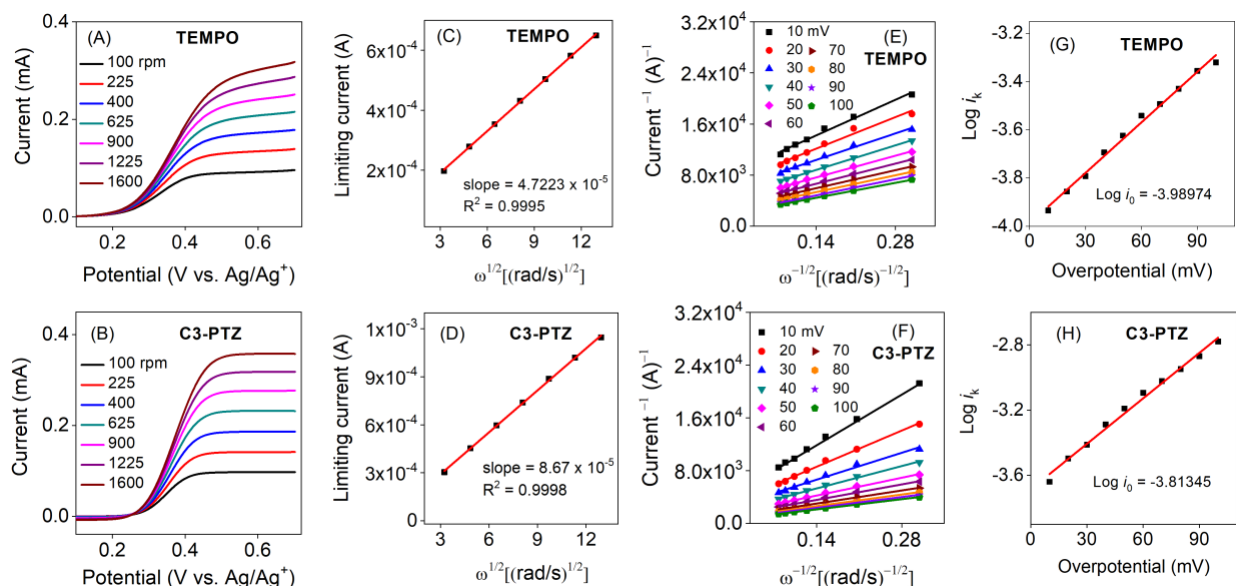
15

Figure 5. Mass transport and kinetic studies of TEMPO and C3-PTZ electrolytes. Linear sweep voltammetry curves of (A) **TEMPO** and (B) **C3-PTZ** at a scan rate of 5 mV/s with rotation rates from 100 to 1600 rpm. Fitted linear Levich plots of the limiting current (i_L) vs. square root of rotation rates ($\omega^{1/2}$) of (C) **TEMPO** and (D) **C3-PTZ**. Linearly fitted Koutecky-Lévich plots of i^{-1} vs. $\omega^{-1/2}$ of (E) **TEMPO** and (F) **C3-PTZ**. Linearly fitted plots of log i_k as a function of overpotential of (G) **TEMPO** and (H) **C3-PTZ**. The rotating disc electrode experiments were performed with 1 mM of redox materials in CH_2Cl_2/$TBAPF_6$ (0.1 M).

Static battery cycling performance

The cycling performance of the membrane-free batteries was first examined under static conditions regarding capacity retention, voltage profiles, and Coulombic/voltage/energy efficiencies. All the charge/discharge experiments were carried out with exposure to air under ambient conditions. As a starting point, the Mg-metal anode was paired with **TEMPO** and **C3-PTZ** redox-active catholytes at concentrations of 0.1 or 0.3 M, resulting in the formation of Mg||**TEMPO** and Mg||**C3-PTZ** MBSBs. Subsequently, both batteries were subjected to charging and discharging for 500 cycles at a current density of 8 mA/cm^2. The schematic illustration and digital photograph of the static battery setup are shown in Figure 6A and Supplementary Figure 9, respectively. Notably, the operational current density exceeded what has been reported for aqueous/nonaqueous (~5 mA/cm^2)[21-23, 25, 27] and nonaqueous/nonaqueous (~2 mA/cm^2)[24,26,28]

16

MBSBs (Supplementary Table S1). The Mg||**TEMPO** (0.1 M) and Mg||**C3-PTZ** (0.1 M) batteries exhibited theoretical capacity utilization of 76.9% and 77.4%, capacity retention of 99.98% (99.999 per cycle, 99.998 per day) (~15 days) and 99.96% (99.999 per cycle, 99.998 per day) (~18 days) (Figures 6B and 6C), and Coulombic efficiencies of 99.63% and 99.43%, voltage efficiencies of 91.24% and 92.15%, and energy efficiencies of 90.56% and 91.31%, respectively (Supplementary Figures 10A and 10B). On the other hand, the Mg||**TEMPO** (0.3 M) and Mg||**C3-PTZ** (0.3 M) batteries exhibit capacity utilization of 71.6% and 72.3%, capacity retentions of 98.91% (99.997 per cycle, 99.974 per day) (~41 days) and 98.42% (99.996 per cycle, 99.965 per day) (~45 days) (Figure 6B and 6C), and Coulombic efficiency of 99.17% and 99.21%, voltage efficiencies of 91.16% and 91.21%, and energy efficiencies of 90.41% and 91.52%, respectively (Supplementary Figure 11A and 11B). All Mg||**TEMPO** (0.1 and 0.3 M) and Mg||**C3-PTZ** (0.1 and 0.3 M) batteries exhibit high capacity retentions and Coulombic efficiencies, confirming the high stability of redox-active materials. Moreover, the high cycling performance of both the MBSBs also highlighted the high reversibility of the Mg metal anode within the developed aqueous anolyte system.
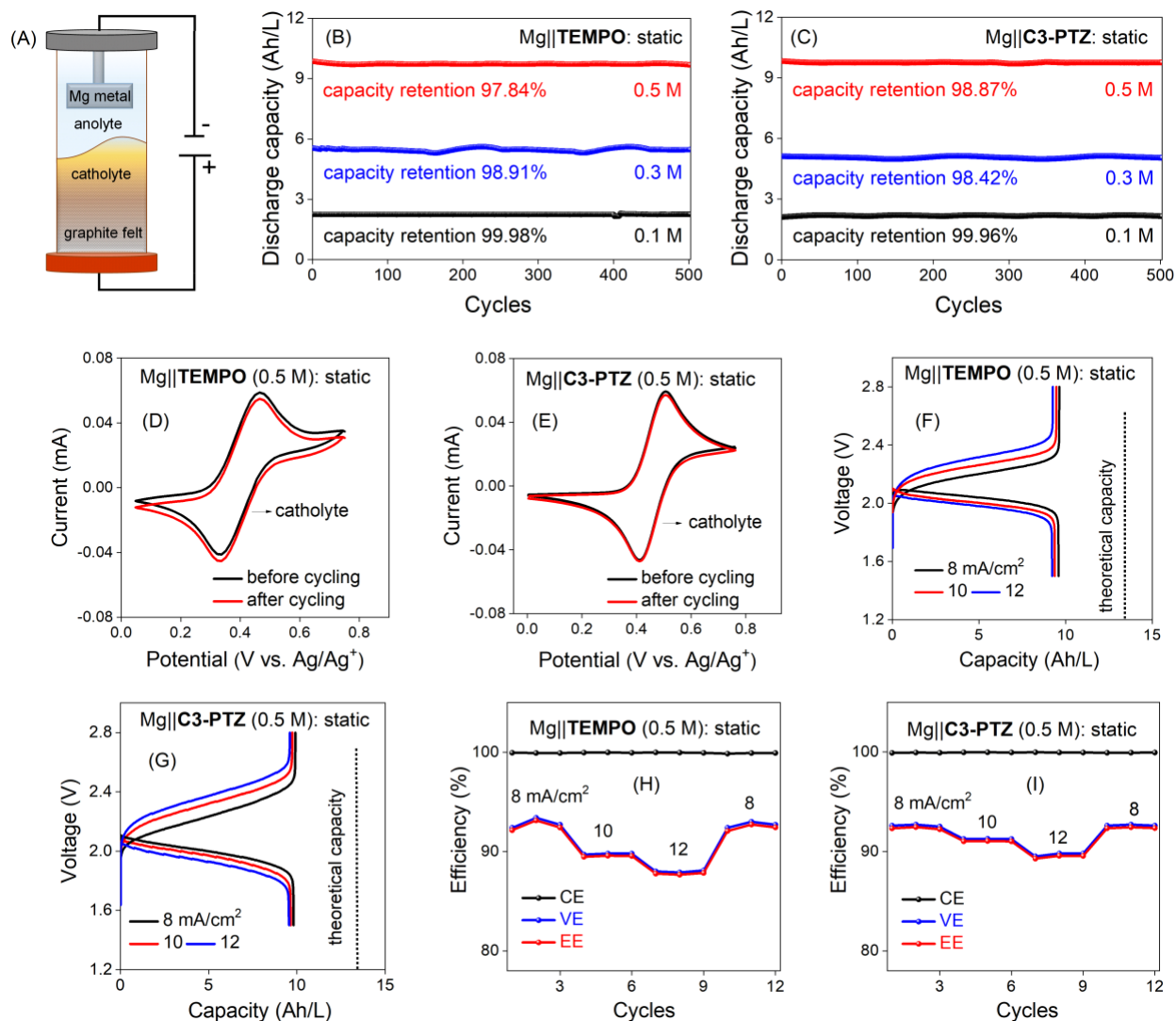
17

Figure 6. Charge/discharge performance of static batteries. Long-term charge/discharge performance of Mg||**TEMPO** (0.5 M) and Mg||**C3-PTZ** (0.5 M) batteries under static conditions. (A) Schematic representation of Mg MBSB static battery. Capacity retention and efficiency evaluation of (B) Mg||**TEMPO** (0.5 M) and (C) Mg||**C3-PTZ** (0.5 M) at the current density of 8 mA/cm^2. CV curves of (D) Mg||**TEMPO** (0.5 M) and (E) Mg||**C3-PTZ** (0.5 M) catholytes before and after long-term battery cycling. Charge/discharge profiles of (F) Mg||**TEMPO** (0.5 M) and (G) Mg||**C3-PTZ** (0.5 M) at different current densities. Variation in Coulombic efficiency (CE), voltage efficiency (VE), and energy efficiency (EE) of (H) Mg||**TEMPO** (0.5 M) and (I) Mg||**C3-PTZ** at different current densities.

To enhance the energy density further, we developed both Mg||**TEMPO** and Mg||**C3-PTZ** MBSBs with higher concentrations of redox-active materials (0.5 M). Both the batteries were tested for long-term charge/discharge performance of 500 cycles. Mg||**TEMPO** (0.5 M) and

18

Mg||**C3-PTZ** (0.5 M) showed good capacity utilization of 70.2% and 71.3%, capacity retention of 97.84% (99.997 per cycle, 99.975 per day) (~73 days) and 98.87% (99.997 per cycle, 99.975 per day) (~79 days) (Figures 6B and 6C), Coulombic efficiencies of 99.17% and 99.12%, voltage efficiencies of 91.52% and 91.61%, and energy efficiency of 91.76% and 90.81% (Supplementary Figure 12A and 12B), respectively. Furthermore, the negligible change in CV current intensity between pre- and post-cycled Mg||**TEMPO** (0.5 M) and Mg||**C3-PTZ** (0.5 M) MBSBs catholytes (Figures 6D and 6E) and anolytes (Supplementary Figure 13A and B) implies the high electrochemical stability of the redox active materials as, well as no crossover of these materials across the liquid/liquid interface throughout the charge/discharge cycling. In addition, both batteries displayed good self-discharge behavior for 170 h (~7 days) (Supplementary Figure 14A and 14B). Low voltage drop over time (0.22 mV/h and 4.3 mV/day for Mg||**TEMPO** (0.5 M), 0.24 mV/h and 5.7 mV/day for Mg||**C3-PTZ** (0.5 M)) further support high stability and high capacity retentions of both batteries under static conditions. Moreover, the electrochemical impedance spectroscopy (EIS) analysis (Supplementary Figure 15A and 15B) of pre-and post-cycled batteries with a negligible change of charge transfer resistance (Rct) confirms the stable performance of battery components, including Mg metal anode and graphite felt, whereas stable solution resistance (Rs) suggests high stability of electrolytes. Therefore, these observations from CV and EIS analysis support the stable performance of both the Mg MBSBs.

In addition to assessing the long-term charge/discharge performance, understanding the charge rate behavior of Mg MBSBs is essential for optimizing performance. It ensures efficient energy storage, prolongs battery life, and enhances safety in practical deployment scenarios. Therefore, to investigate the charge rate behaviors, both the Mg||**TEMPO** (0.5 M) and Mg||**C3-PTZ** (0.5 M) MBSBs were subjected to charging/discharging under static conditions at varied

current densities of 8, 10, and 12 mA/cm^2. With increased current density, both batteries exhibited increased overpotential during charge and discharge (Figures 6F and 6G), attributed to mass diffusion limitation. Both the Mg||**TEMPO** (0.5 M) and Mg||**C3-PTZ** (0.5 M) batteries exhibited consistently high Coulombic efficiencies of ~99.23% and ~99.34%, respectively, across all operating current densities. This suggests minimal side reactions during fast charging/discharging (Figure 6H and 6I). However, there was a notable decrease in energy efficiency values, from 91.52% to 87.21% for Mg||**TEMPO** (0.5 M) and from 92.12% to 88.33% for Mg||**C3-PTZ** (0.5 M). This decline was attributed to an increase in overpotential caused by mass transport losses. Importantly, both Mg MBSBs regained their original efficiencies when cycled back at 8 mA/cm^2, confirming their high charge-rate performance.

Since mass transport limitations affect energy delivery, monitoring the evolution of power density becomes crucial in improving battery efficiency and practicality. Therefore, power density analysis for the Mg||**TEMPO** (0.5) and Mg||**C3-PTZ** (0.5) static MBSBs was carried out at different states of charge (SOCs). At a SOC of 100%, the peak power densities of the Mg||**TEMPO** (0.5 M) and Mg||**C3-PTZ** (0.5 M) batteries were measured to be 139 and 144 mW/cm², respectively (Supplementary Figures 16A and 16B). In addition, the values of area-specific resistance (ASR) were investigated for both the electrolyte and the entire cell (Supplementary Figures 16C and 16D). Notably, ASR decreased with increasing SOC, with electrolyte resistance contributing ~70% and ~72% to the overall cell resistance for Mg||**TEMPO** (0.5 M) and Mg||**C3-PTZ** (0.5 M), respectively. These low ASR values enables batteries to operate even at a high current density of 12 mA/cm^2 as compared to the earlier reported membrane-free battery system (Supplementary Table 2)[21-28].

Battery cycling performance under stirring and flow conditions

While the static batteries demonstrated high cycling performance, their capacity utilization was limited due to mass transport. In addition, static batteries do not possess the advantage of decoupled energy and power of redox flow batteries. A recent study by Meng et al.[23] reported a stirred strategy to enhance mass transport and increase battery capacity utilization. Hence, we also adopted the stirring technique for both Mg||**TEMPO** (0.5 M) and Mg||**C3-PTZ** (0.5M) MBSBs. This resulted in improved capacity utilization of 92.4% for Mg||**TEMPO** (0.5 M) and 93.8% for Mg||**C3-PTZ** (0.5 M) (Figure 7A and 7B) from 70.2% and 71.5% for the corresponding 0.5 M static MBSBs, respectively. Moreover, both Mg||**TEMPO** (0.5 M) and Mg||**C3-PTZ** (0.5 M) stirred MBSBs were performed for 200 charge/discharge cycles, exhibiting capacity retention of 99.82% (99.999 per cycle, 99.994 per day) (~35 days) and 99.88% (99.999 per cycle, 99.996 per day) (~39 days) for both batteries Coulombic efficiencies of 99.51% and 99.58%, voltage efficiencies of 92.82% and 93.15%, and energy efficiencies of 92.36% and 92.78%, respectively. Further, the negligible change in CV current intensity of both the batterie's catholytes (Figures 7C and 7D) and anolytes (Supplementary Figures 17A and 17B) demonstrated high stability, as well as negligible crossover of redox-active materials. In addition, the EIS analysis of both stirred batteries before and after cycling confirms stable kinetics (Supplementary Figure 18). Furthermore, both stirred batteries were investigated for charge-rate test by varying current density from 10 to 15 mA/cm^2. The Mg||**TEMPO** (0.5 M) and Mg||**C3-PTZ** (0.5 M) stirred batteries exhibited a slight increase/decrease in charge/discharge voltage with an increase in current density due to mass transport limitations (Figures 7E and 7F). As a result, Mg||**TEMPO** (0.5 M) and Mg||**C3-PTZ** (0.5 M) stirred batteries operated at higher current densities (12.5 and 15 mA/cm^2) exhibited reduced values of energy efficiencies (Figures 7G and 7H). However, both batteries

regained initial efficiency values and cycling performance when cycled back at 10 mA/cm^2, demonstrating high charge/discharge rate behavior.
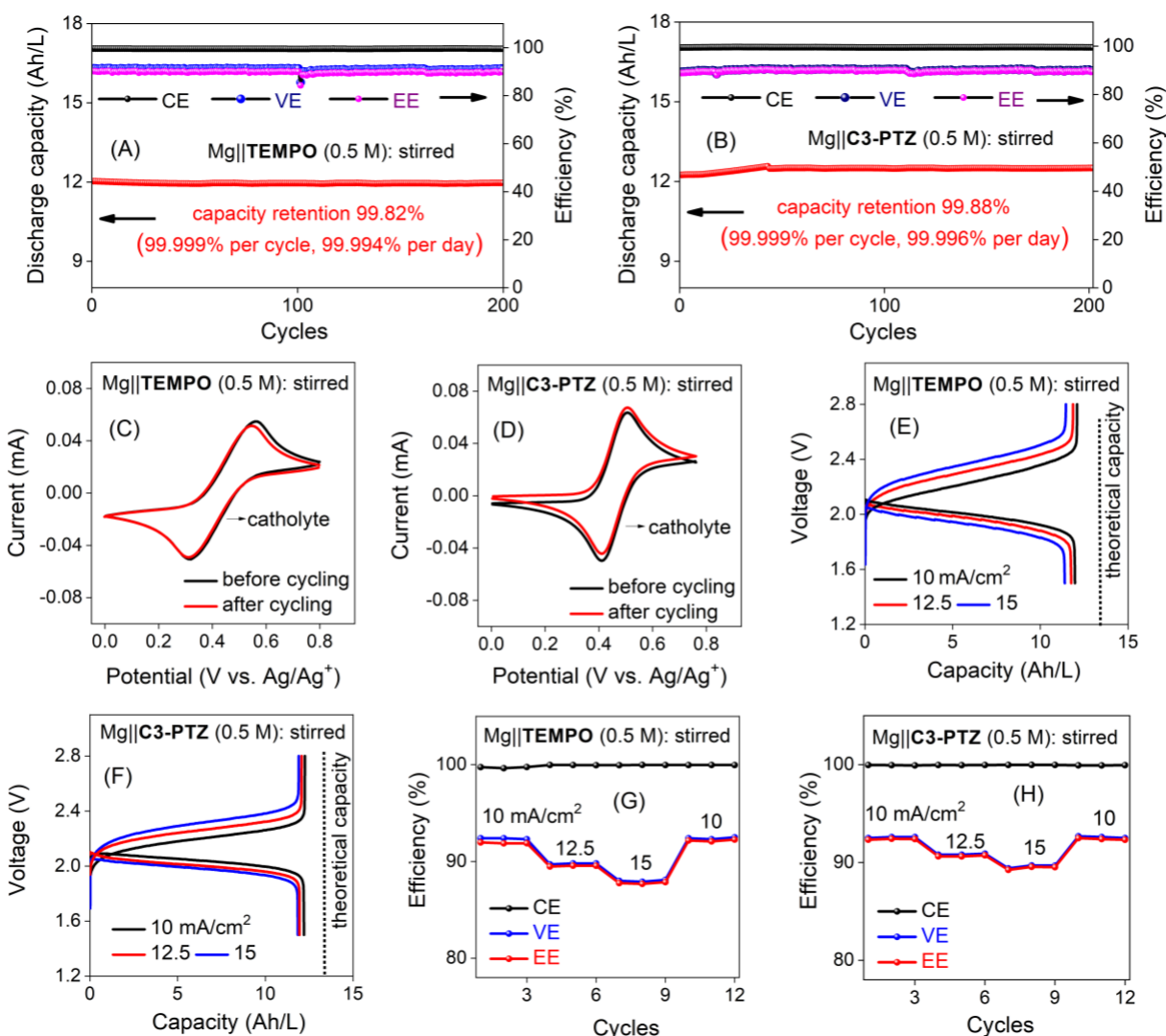

Figure 7. Charge/discharge performance of stirred batteries Long-term charge/discharge performance of Mg||**TEMPO** and Mg||**C3-PTZ** MBSBs under stirred conditions. Capacity retention and efficiency of (A) Mg||**TEMPO** (0.5 M) and (B) Mg||**C3-PTZ**, both batteries were operated at a charge/discharge current density of 10 mA/cm^2. CV curves of (D) Mg||**TEMPO** (0.5 M) and (E) Mg||**C3-PTZ** (0.5 M) catholytes before and after long-term battery cycling. Charge/discharge profiles of (F) Mg||**TEMPO** (0.5 M) and (G) Mg||**C3-PTZ** (0.5 M) at different current densities. Variation in Coulombic efficiency (CE), voltage efficiency (VE), and energy efficiency (EE) of (H) Mg||**TEMPO** (0.5 M) and (I) Mg||**C3-PTZ** at different current densities.

22

Although the stirred batteries demonstrated enhanced mass transport and increased capacity utilization, the battery scalability remains limited due to coupled energy and power characteristics[21]. To overcome such limitations, we further investigated the Mg||**TEMPO** (0.5 M) and Mg||**C3-PTZ** (0.5 M) batteries under flow conditions. The schematic illustration and digital photograph of the flow setup are shown in Figure 8A and Supplementary Figure 19. All the charge/discharge experiments were carried out with exposure to air under ambient conditions. This study marks the first time an Mg-metal-based membrane-free biphasic redox flow battery, enabling the advantage of decoupled energy and power. The flow rate of both batteries was optimized between 1 and 5 mL/min. Both batteries exhibit optimal performance at a flow rate of 3 mL/min (Supplementary Figure 20). The charge/discharge performance of both batteries was explored for 500 cycles at 12 mA/cm^2 under ambient conditions at an optimized flow rate of 3 mL/min. After 500 charge/discharge cycles, the Mg||**TEMPO** (0.5 M) and Mg||**C3-PTZ** (0.5 M) redox flow MBSBs exhibited capacity utilization of 92.2% and 91.7%, retention of 93.58% (99.987 per cycle, 99.924 per day) (~85 days) and 92.16% (99.984 per cycle, 99.903 per day) (~81 days), Coulombic efficiency of 99.8% and 99.7%, voltage efficiency of 93.5% and 92.2%, and energy efficiency of 92.8% and 91.9%, respectively (Figure 8B and 8C). The high capacity retentions of both batteries were attributed to the negligible crossover of redox-active materials as confirmed by the CV analysis of pre- and post-cycled catholytes (Figures 8D and 8E) and anolytes (Supplementary Figures 21A and 21B). Excellent self-discharge performance was also observed for both batteries for a long duration of 170 h (7 days). Low voltage drop over time (0.72 mV/h and 16.3 mV/day for Mg||**TEMPO**, 0.68 mV/h and 15.7 mV/day for Mg||**C3-PTZ**) (Supplementary Figures 22A and 22B) further support high stability of Mg metal anode as well as the catholyte materials. The EIS analysis of Mg||**TEMPO** (0.5 M) and Mg||**C3-PTZ** (0.5 M) before and after flow cycling

23

displayed no major change in the charge-transfer resistance, suggesting that the kinetics of the system remain intact (Supplementary Figure 23). The result also confirms the Mg-metal anode forms no passivation layer of $Mg(OH)_2$, which is attributed to the excellent stability of the Mg^{2+}-conducting interface and improved Mg reversibility in the aqueous Mg-electrolyte.
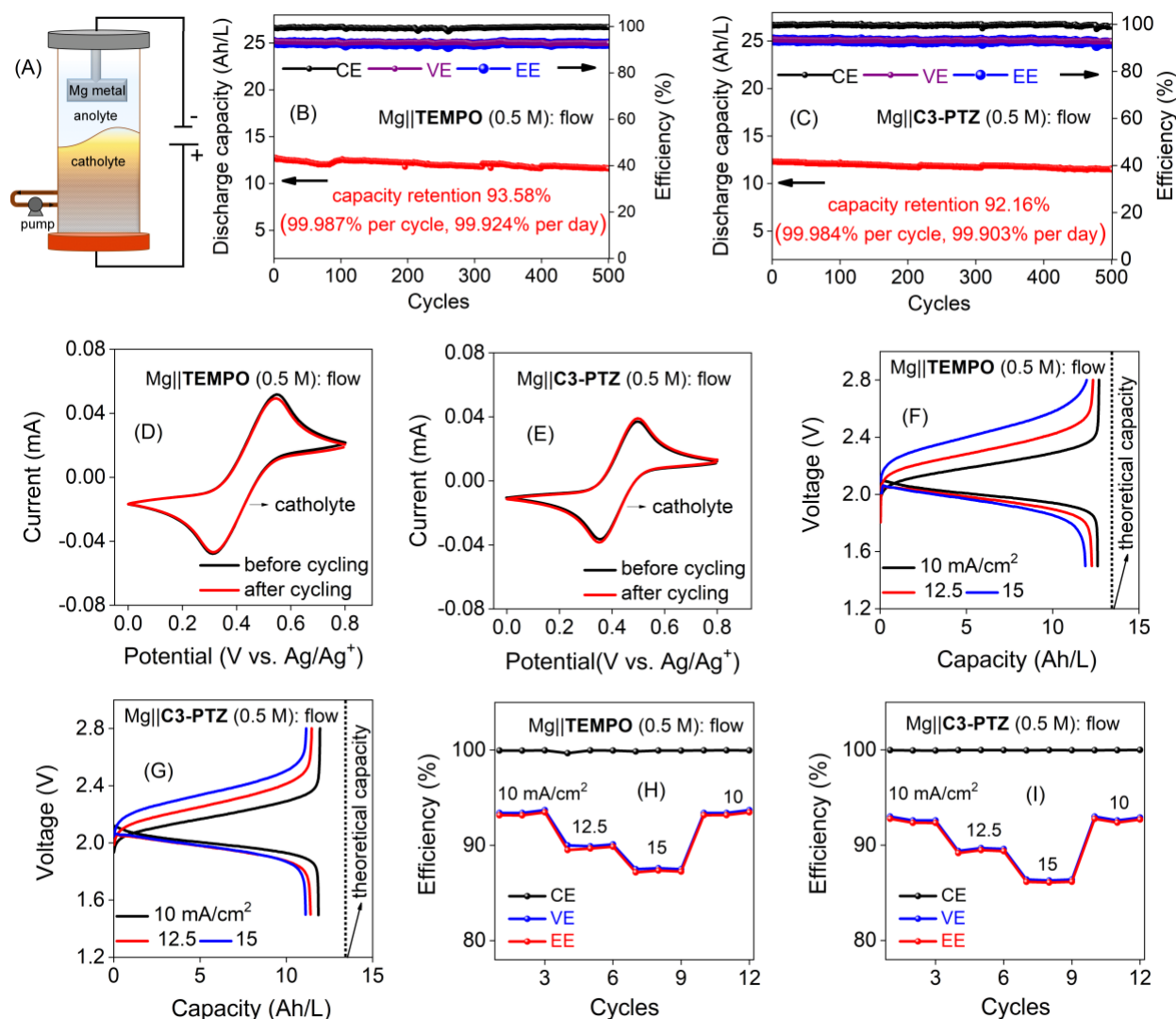

Figure 8. Charge/discharge performance of flow batteries Long-term charge/discharge performance of Mg‖**TEMPO** (0.5 M) and Mg‖**C3-PTZ** (0.5 M) MBSBs under flow conditions. (A) Schematic representation of Mg BSMB flow battery. Capacity retention and efficiency of (B) Mg‖**TEMPO** (0.5 M) and (C) Mg‖**C3-PTZ** (0.5 M) at the current density of 10 mA/cm². CV curves of (D) Mg‖**TEMPO** (0.5 M) and (E) Mg‖**C3-PTZ** (0.5 M) catholytes before and after long-term battery cycling. Charge/discharge profiles of (F) Mg‖**TEMPO** (0.5 M) and (G) Mg‖**C3-PTZ** (0.5 M) at different current densities. Variation in Coulombic efficiency (CE), voltage efficiency

(VE), and energy efficiency (EE) of (H) Mg||**TEMPO** (0.5 M) and (I) Mg||**C3-PTZ** at different current densities.

To study the effects of varied current density on battery performance, the Mg||**TEMPO** (0.5 M) and Mg||**C3-PTZ** (0.5 M) battery was charged/discharged at different current densities of 10, 12.5, and 15 mA/cm^2, and the corresponding cycling profiles, as well as Coulombic efficiency, voltage efficiency, and energy efficiency, were recorded (Figures 8F and 8G). It is observed that both batteries result in increased charge/discharge overpotential when operated at higher current densities of 12.5 and 15 mA/cm^2 due to mass transport limitations (Figures 8H and 8I). Both the batteries regained their original performance when cycled back at 10 mA/cm^2, suggesting high rate cyclability under flow conditions. Power densities were also measured for both batteries under flow conditions. The peak power density of Mg||**TEMPO** (0.5 M) and Mg||**C3-PTZ** (0.5 M) batteries achieved 195 and 191 mW/cm^2, respectively (Supplementary Figures 24A and 24B), surpassing the power densities of 139 mW/cm^2 for Mg||**TEMPO** and 144 mW/cm^2 for Mg||**C3-PTZ** under static conditions. The improvement in power can be attributed to enhanced mass transport under flow conditions. the ASR of electrolyte resistance and the whole cell under flow conditions revealed that electrolyte resistance contributed to over 70% (Mg||**TEMPO**) and 65% (Mg||**C3-PTZ)** of the total battery resistance (Supplementary Figures 24C and 24D). Under flow conditions, both the electrolyte and overall ASR notably decreased compared to static MBSBs, enabling higher current and power densities without compromising battery performance.

Economic analysis

The cost of RFBs plays a pivotal role in practical application. Generally, the total cost of an RFB includes several key components: the membrane, carbon electrode, active materials, electrolyte and its salt, bipolar plate, current collector plate, the pump to circulate the electrolyte, gasket, bolts,

and endplates[59,60]. The cost distribution among major components of RFB varies, with the membrane accounting for 20–30%, the bipolar plate 15–20%, the carbon electrode 10–15%, active materials (anode and cathode) usually 20-50%, the current collector plate 5–10%, and miscellaneous components such as pumps, endplates, gaskets, bolts, etc., comprising around 2-5%[61,62]. The aqueous electrolyte, with their almost negligible cost ($0.1/kg), compose <2% of the total cost of aqueous redox flow batteries (ARFBs, all-vanadium, zinc-bromine, zinc-ferricyanide, etc.)[61]. In contrast, the significantly higher cost of nonaqueous electrolyte ($3/L) and its salt ($5/kg) makes up 20–35% of the total cost of nonaqueous redox flow batteries (NRFB, Li-TEMPO)[60,61]. These estimations result in a substantial difference in capital costs, with the cost of NRFB (Li-TEMPO) at $1237/kWh, which is five times higher than that of all-vanadium ARFB at $252/kWh[61]. The present system is an aqueous/nonaqueous membrane-free system, thus the cost of a membrane is avoided. It utilizes water and Mg metal ($2/kg) as an inexpensive anolyte phase and CH_2Cl_2 with redox materials (**TEMPO** and **C3-PTZ**) as a catholyte phase. The solvent cost of CH_2Cl_2 (~$20/L)[63] is approximately 60 times lower than carbonate-based nonaqueous electrolytes (~$1200/L)[64]. In addition, the cost of major anolyte and catholyte salts, $MgCl_2$ (~$68/kg)[65] and $TBAPF_6$ (~$2000/kg)[66] respectively, is significantly cheaper compared to Li-based salts (LiTFSI at ~$4000/kg[67], $LiPF_6$ at ~$3800/kg[64]) used in NRFBs. Furthermore, the cost of **TEMPO** ($7000/Kg)[68] and **C3-PTZ** (~$133/kg)[26], is comparable to the cost of active materials (~$256/kg, vanadium)[69] used in ARFBs. In addition, the developed battery system is feasible to operate in open-air conditions, avoiding the need for an air-free chamber, such as an argon-filled glovebox. Altogether, the present membrane-free system demonstrates significantly lower costs compared to both all-vanadium ARFBs and TEMPO-based NRFBs.

Conclusion

26

This work introduces a newly developed high-voltage liquid/liquid membrane-free battery employing Mg metal anode in both static and flow configurations. This system leverages the advantages of the high voltage and fast kinetics by Mg metal anode within a biphasic membrane-free flow setup to enable independent optimization of energy and power. The biphasic system utilizes a CH_2Cl_2 catholyte and an aqueous anolyte containing ethylene glycol and ionic liquid additives to address the passivation issue of Mg metal in traditional electrolyte systems. In addition, a Mg^{2+} conductive interface was implemented to modify the Mg-metal electrode, preventing direct contact between Mg metal and water molecules to further mitigate the passivation issue. Notably, the batteries operated in ambient atmospheric conditions showcasing remarkable oxygen tolerance. The Mg||**TEMPO** and Mg||**C3-PTZ** batteries were tested in static, stirred, and flow conditions. Initial analysis focused on their charge/discharge performance with different catholyte material concentrations. Notably, the Mg||**TEMPO** (0.5 M) and Mg||**C3-PTZ** (0.5 M) batteries exhibited exceptional performance over 500 cycles, with capacity retention rates of 97.84% and 98.87% (under static conditions) and 93.58% and 92.16% (under flow conditions), respectively. In addition, both Mg||**TEMPO** (0.5 M) and Mg||**C3-PTZ** (0.5 M) under flow conditions outperformed the power performance in static configuration, demonstrating power densities of 195 and 191 mW/cm^2, respectively. Overall, the newly developed cost-effective Mg MBSBs exhibited remarkable battery performance, paving the way for innovative applications of Mg chemistry in flow batteries.

Methods

Materials

27

Magnesium chloride ($MgCl_2$, 98%), magnesium bis(trifluoromethanesulfonimide) (Mg(TFSI)$_2$), 99.98%), dichloromethane (CH_2Cl_2, HPLC grade), ethylene glycol (EG, 99%), were used without further purification.

Electrochemical characterization

For CV measurements, solutions of **TEMPO** and **C3-PTZ** (5 mM) were prepared in a CH_2Cl_2/TBAPF$_6$ (0.1 M) electrolyte. A glassy carbon disk (CHI Instrument, 3 mm) was used as the working electrode and was polished with Al_2O_3 (Pine Research Instrumentation, Inc., 5 mm) using water as the solvent before the measurements. A piece of Pt wire (Pine Research Instrumentation, Inc., thickness 0.5 mm, purity 99.99%) was used as the counter electrode, and an Ag/Ag$^+$ electrode (Fisher Scientific) served as the reference electrode. CV measurements were performed using a Bio-Logic potentiostat. EIS was conducted with an applied potentiostatic signal ranging from 200 KHz to 100 mHz with an amplitude of 10 mV. The measurements were conducted under open-circuit voltage (OCV) conditions, yielding a total of 54 data points. Charge/discharge performances were evaluated using Land and Bio-Logic potentiostats. The LSV was employed to measure the ASR of static and flow cells. ASR was determined by conducting LSV experiments on batteries containing various redox materials. The results were presented as polarization curves, with the current (i) plotted against the applied potential (V). By carefully analyzing these curves, a linear region was identified where the current response exhibited a direct proportionality to the applied potential. This analysis allowed the calculation of the differential resistance (dE/di), typically observed at low overpotentials, indicating a kinetic-limited regime of electrochemical reactions. The ASR assessment involved extracting the slope (S) of the linear region within the polarization curve. Using the formula (ASR = 1/S), the area-specific resistance was calculated, which represents the resistance normalized to the electrode area. To ensure the

28

experiment's reliability and reproducibility, the same electrochemical characterizations were performed on two distinct sets of cells. The LSV investigations were conducted using a Pine modulated speed rotator paired with Biologic potentiostats. In this setup, an RDE with a diameter of 5 mm served as the working electrode, while a Pt wire electrode and an Ag/Ag^+ electrode were utilized as the counter and reference electrodes, respectively. To ensure consistent and controlled conditions, the samples underwent a purging process with 99.999% pure argon for 20 minutes before the testing commenced. LSV data was collected at various rotation rates, spanning from 100 to 1600 rpm. The diffusion coefficient (D_o) of electroactive materials was calculated from the Lévich plot using Equation 1[50];

$$I = 0.62nFAC_oD^{2/3}\omega^{1/2}\upsilon^{-1/6} \tag{1}$$

Where i is limiting current density, n is the number of electrons in the redox process, F is Faraday's constant, A is the area of the glassy carbon electrode, C_0 is the concentration of active material, ω is angular rotation rate, and υ is the kinematic viscosity of CH_2Cl_2/TBAPF$_6$ (0.1 M) solution. The kinetic rate constant is calculated by Equation 2.

$$i_0 = FAC_0k_0 \tag{2}$$

Where i_0 was calculated from the fitting line of the Butler-Volmer equation, the x-intercept is the log of the exchange current i_0 (0.0003 A), F is Faraday's constant, A is the area of the glassy carbon electrode (0.196 cm^2), C_0 is the concentration of redoxmers (0.5×10^{-6} mol/cm^3), k_0 is reaction rate constant (cm/s).

The corrosion experiments of Mg/MgCl$_2$ (1 M), Mg/WEIL, and PC-Mg/WEIL systems were conducted at a scan rate of 10 mV/s. To determine the corrosion current (I_{corr}), Tafel extrapolation was performed on the cathodic polarization curves. For these experiments, Mg or PC-Mg served as the working electrode, Pt was employed as the counter electrode, and Ag/AgCl

29

was used as the reference electrode. The electrolytes were either $MgCl_2$ (1 M) or WEIL.The charge/discharge performance of Mg||**TEMPO** and Mg||**C3-PTZ** batteries, both in static and flow configurations, was evaluated using Land and Bio-Logic potentiostats. These assessments were conducted over an extended period of 500 cycles, with a charge cutoff voltage of 2.8 V and a discharge cutoff voltage of 1.5 V. The constant current density applied was 8 mA/cm^2 for static batteries and 12 mA/cm^2 for flow batteries. For static battery studies, 0.25 mL of catholyte and 0.25 mL of anolyte were used. In contrast, flow battery studies involved 0.5 mL of catholyte and 0.5 mL of anolyte, with the catholyte being circulated through the cell at a flow rate of 3 mL/min using a peristaltic pump. To analyze the rate performance, both static and flow batteries were subjected to different current densities: 8, 10, and 12 mA/cm^2 for static batteries, and 10, 12.5, and 15 mA/cm^2 for flow batteries. Each current density was tested with three charge/discharge cycles. In addition, the self-discharge performance of the flow battery was evaluated by monitoring OCV overtime on a fully charged battery.

To assess the reversible stability of Mg or PC-Mg metal anodes, symmetrical batteries configured as Mg|Mg $MgCl_2$ (1 M), Mg|Mg (WEIL), and PC-Mg|PC-Mg (WEIL) were cycled at a current density of 0.5 mA/cm^2, with each cycle lasting 20 minutes.**Measurement of capacity utilization and retention**

The capacity utilization of the battery was calculated as the ratio of the operational battery capacity (C_b) to its theoretical capacity (C_t) at a specific SOC. The SOC was defined based on the duration of battery charge or discharge cycles.

Capacity utilization (%) = [C_b (charge or discharge)/C_t] x 100

On the other hand, capacity retention was determined by normalizing the discharge capacity during cycling. Here, C_i represents the discharge capacity obtained in the first cycle, while C_f represents the discharge capacity obtained in subsequent cycles.

Capacity retention (%) = $[C_f/C_i]$ x 100

Solubility test

To determine the solubility of redox-active cathode materials, a solution of CH_2Cl_2/TBAPF$_6$ (1.5 M) was employed. The solution was incrementally added to a vial containing known quantities of redox materials. The addition continued until a clear solution was achieved, at which point the volume of the electrolyte was measured using an analytical pipette. Subsequently, the solubility of the organic compounds was calculated by finding the ratio of the molar amount of cathode materials to the volume of the electrolyte. This entire process was repeated twice to ensure accuracy, and the averaged values of the solubility were presented.

Development of the biphasic system

Four aqueous/nonaqueous biphasic systems were developed including water/CH_2Cl_2, water/fluoroethylene carbonate (FEC), EG/FEC, and water/1-butyl-1-methylpyrrolidinium bis(trifluoromethylsulfonyl)imide. Although all the system shows high compatibility with Mg metal and cathode redox materials, water/CH_2Cl_2 is more cost-effective compared to other systems, hence is selected for battery performance studies.

Data availability

Most data supporting the findings of this study are included in the main text of the article and its Supplementary Information. Raw datasets can be obtained from the corresponding author on request.

https://doi.org/10.26434/chemrxiv-2024-vrn3h ORCID: https://orcid.org/0000-0002-7466-522X Content not peer-reviewed by ChemRxiv. **License:** CC BY-NC 4.0

Acknowledgements

References

1. Dunn, B., Kamath, H. & Tarascon, J. M. Electrical energy storage for the grid: a battery of choices. *Science* **334**, 928–935 (2011).
2. Larcher, D. & Tarascon, J. M. Towards greener and more sustainable batteries for electrical energy storage. *Nat. Chem.* **7**, 19–29 (2015).
3. Kittner, N., Lill, F. & Kammen, D. M. Energy storage deployment and innovation for the clean energy transition. *Nat. Energy* **2**, (2017).
4. Tian, Y., *et al.* Promises and challenges of next-generation "beyond Li-ion" batteries for electric vehicles and grid decarbonization. *Chem. Rev.* **121**, 1623–1669 (2021).
5. Masias, A., Marcicki, J. & Paxton, W. A. Opportunities and challenges of lithium ion batteries in automotive applications. *ACS Energy Lett.* **6**, 621–630 (2021).
6. Winter, M., Barnett, B. & Xu, K. Before Li ion batteries. *Chem. Rev.* **118**, 11433–11456 (2018).
7. Saha, P., *et al.* Rechargeable magnesium battery: Current status and key challenges for the future. *Prog. Mater Sci.* **66**, 1–86 (2014).
8. Leong, K. W., *et al.* Reversibility of a high-voltage, Cl⁻regulated, aqueous Mg metal battery enabled by a water-in-salt electrolyte. *ACS Energy Lett.* **7**, 2657–2666 (2022).
9. Liu, F., Wang, T., Liu, X. & Fan, L. Z. Challenges and recent progress on key materials for rechargeable magnesium batteries. *Adv. Energy Mater.* **11**, (2020).
10. Qin, Y., Holguin, K., Fehlau, D., Luo, C. & Gao, T. Nonaqueous Mg flow battery with a polymer catholyte. *ACS Appl. Energy Mater.* **5**, 2675–2678 (2022).
11. He, P., *et al.* Stability and disproportionation of magnesium polysulfides and the effects on the Mg-polysulfide flow battery. *J. Electrochem. Soc.* **168**, (2021).
12. Soloveichik, G. L. Flow batteries: Current status and trends. *Chem. Rev.* **115**, 11533–11558 (2015).
13. Hou, S., *et al.* High-energy and low-cost membrane-free chlorine flow battery. *Nat. Commun.* **13**, 1281 (2022).
14. Ye, C., *et al.* Long-life aqueous organic redox flow batteries enabled by amidoxime-functionalized ion-selective polymer membranes. *Angew. Chem. Int. Ed.* **61**, e202207580 (2022).
15. Liang, Y., Dong, H., Aurbach, D. & Yao, Y. Current status and future directions of multivalent metal-ion batteries. *Nat. Energy* **5**, 646–656 (2020).
16. Deivanayagam, R., Ingram, B. J. & Shahbazian-Yassar, R. Progress in development of electrolytes for magnesium batteries. *Energy Storage Mater.* **21**, 136–153 (2019).
17. Navalpotro, P., *et al.* Critical aspects of membrane-free aqueous battery based on two immiscible neutral electrolytes. *Energy Storage Mater.* **26**, 400–407 (2020).
18. Navalpotro, P., *et al.* Exploring the versatility of membrane-free battery concept using different combinations of immiscible redox electrolytes. *ACS Appl. Mater. Interfaces* **10**, 41246–41256 (2018).
19. Peljo, P., Bichon, M. & Girault, H. H. Ion transfer battery: storing energy by transferring ions across liquid-liquid interfaces. *Chem. Commun.* **52**, 9761–9764 (2016).
20. Xu, P., *et al.* A membrane-free interfacial battery with high energy density. *Chem. Commun.* **54**, 11626–11629 (2018).
21. Navalpotro, P., Palma, J., Anderson, M. & Marcilla, R. A membrane-free redox flow battery with two immiscible redox electrolytes. *Angew. Chem. Int. Ed.* **56**, 12460–12465 (2017).

22. Navalpotro, P., *et al.* Pioneering use of ionic liquid-based aqueous biphasic systems as membrane-free batteries. *Adv. Sci.* **5**, 1800576 (2018).

23. Meng, J., *et al.* A stirred self-stratified battery for large-scale energy storage. *Joule* **4**, 953–966 (2020).

24. Wang, Z., *et al.* Exploiting nonaqueous self-stratified electrolyte systems toward large-scale energy storage. *Nat. Commun.* **14**, 2267 (2023).

25. Chai, J., *et al.* Biphasic, membrane-free Zn/phenothiazine battery: effects of hydrophobicity of redox materials on cyclability. *ACS Mater. Lett.* **3**, 337–343 (2021).

26. Gautam, R. K., *et al.* Development of high-voltage and high-energy membrane-free nonaqueous lithium-based organic redox flow batteries. *Nat. Commun.* **14**, 4753 (2023).

27. Wang, X., Lashgari, A., Chai, J. & Jiang, J. A membrane-free, aqueous/nonaqueous hybrid redox flow battery. *Energy Storage Mater.* **45**, 1100–1108 (2022).

28. Gautam, R. K., Wang, X., Sinha, S. & Jiang, J. Triphasic electrolytes for membrane-free high-voltage redox flow battery. *ACS Energy Lett.* **9**, 218–225 (2023).

29. Navalpotro, P., Ibañez, S. E., Pedraza, E. & Marcilla, R. A neutral pH aqueous biphasic system applied to both static and flow membrane-free battery. *Energy Storage Mater.* **56**, 403–411 (2023).

30. Pour, N., Gofer, Y., Major, D. T. & Aurbach, D. Structural analysis of electrolyte solutions for rechargeable Mg batteries by stereoscopic means and DFT calculations. *J. Am. Chem. Soc.* **133**, 6270–6278 (2011).

31. Gao, T., *et al.* Reversible S^0/MgS_x redox chemistry in a $MgTFSI_2/MgCl_2/DME$ electrolyte for rechargeable Mg/S batteries. *Angew. Chem. Int. Ed.* **56**, 13526–13530 (2017).

32. Canepa, P., *et al.* Elucidating the structure of the magnesium aluminum chloride complex electrolyte for magnesium-ion batteries. *Energy Environ. Sci.* **8**, 3718–3730 (2015).

33. See, K. A., *et al.* The Interplay of Al and Mg speciation in advanced Mg battery electrolyte solutions. *J. Am. Chem. Soc.* **138**, 328–337 (2016).

34. He, S., Luo, J. & Liu, T. L. $MgCl_2/AlCl_3$ electrolytes for reversible Mg deposition/stripping: electrochemical conditioning or not? *J. Mater. Chem. A* **5**, 12718–12722 (2017).

35. Kim, S. S., Bevilacqua, S. C. & See, K. A. Conditioning-free Mg electrolyte by the minor addition of $Mg(HMDS)_2$. *ACS Appl. Mater. Interfaces* **12**, 5226–5233 (2020).

36. Liao, C., *et al.* The unexpected discovery of the $Mg(HMDS)_2/MgCl_2$ complex as a magnesium electrolyte for rechargeable magnesium batteries. *J. Mater. Chem. A* **3**, 6082–6087 (2015).

37. Shterenberg, I., *et al.* Evaluation of $(CF_3SO_2)_2N^-$ (TFSI) based electrolyte solutions for Mg batteries. *J. Electrochem. Soc.* **162**, A7118–A7128 (2015).

38. Mohtadi, R., Tutusaus, O., Arthur, T. S., Zhao-Karger, Z. & Fichtner, M. The metamorphosis of rechargeable magnesium batteries. *Joule* **5**, 581–617 (2021).

39. Ng, K. L., Shu, K. & Azimi, G. A rechargeable $Mg|O_2$ battery. *iScience* **25**, 104711 (2022).

40. Vardar, G., *et al.* Electrochemistry of magnesium electrolytes in ionic liquids for secondary batteries. *ACS Appl. Mater. Interfaces* **6**, 18033–18039 (2014).

41. Chellappan, L. K., *et al.* Non-nucleophilic electrolyte based on ionic liquid and magnesium bis(diisopropyl)amide for rechargeable magnesium-ion batteries. *ACS Appl. Energy Mater.* **3**, 9585-9593 (2020).

42. Kakibe, T., Hishii, J.-y., Yoshimoto, N., Egashira, M. & Morita, M. Binary ionic liquid electrolytes containing organo-magnesium complex for rechargeable magnesium batteries. *J. Power Sources* **203**, 195–200 (2012).

43. Watkins, T., Kumar, A. & Buttry, D. A. Designer ionic liquids for reversible electrochemical deposition/dissolution of magnesium. *J. Am. Chem. Soc.* **138**, 641–650 (2016).

44. Tan, J. & Liu, J. Electrolyte engineering toward high-voltage aqueous energy storage devices. *Energy Environ. Mater.* **4**, 302–306 (2020).

45. Wang, F., *et al.* High-voltage aqueous magnesium ion batteries. *ACS Cent Sci* **3**, 1121–1128 (2017).

46. Fu, Q., *et al.* High-voltage aqueous Mg-ion batteries enabled by solvation structure reorganization. *Adv. Funct. Mater.* **32**, 2110674 (2022).

47. Shen, Y., *et al.* Water-in-salt electrolyte for safe and high-energy aqueous battery. *Energy Storage Mater.* **34**, 461–474 (2021).

48. Ma, Z., Kar, M., Xiao, C., Forsyth, M. & MacFarlane, D. R. Electrochemical cycling of Mg in Mg[TFSI]$_2$ /tetraglyme electrolytes. *Electrochem. Commun.* **78**, 29–32 (2017).

49. Zhang, Y., Ye, R., Henkensmeier, D., Hempelmann, R. & Chen, R. "Water-in-ionic liquid" solutions towards wide electrochemical stability windows for aqueous rechargeable batteries. *Electrochim. Acta* **263**, 47–52 (2018).

50. Xie, J., Liang, Z. & Lu, Y. C. Molecular crowding electrolytes for high-voltage aqueous batteries. *Nat. Mater.* **19**, 1006–1011 (2020).

51. Huang, S., *et al.* Ultrahigh-voltage aqueous electrolyte for wide-temperature supercapacitors. *J. Mater. Chem. A* **11**, 15532–15539 (2023).

52. Song, G. & StJohn, D. Corrosion behaviour of magnesium in ethylene glycol. *Corrosion Science* **46**, 1381–1399 (2004).

53. Lopez, J., *et al.* Effects of polymer coatings on electrodeposited lithium metal. *J. Am. Chem. Soc.* **140**, 11735–11744 (2018).

54. Wang, Y., *et al.* Optimizing the sulfonic groups of a polymer to coat the zinc anode for dendrite suppression. *Chem. Commun.* **57**, 5326–5329 (2021).

55. Wu, Q., Shu, K., Sun, L. & Wang, H. Recent advances in non-nucleophilic Mg electrolytes. *Front. Mater.* **7**, 612134 (2021).

56. Nguyen, D.-T., *et al.* A high-performance magnesium triflate-based electrolyte for rechargeable magnesium batteries. *Cell Rep. Phys. Sci.* **1**, 100265 (2020).

57. Chen, J., *et al.* The Metamorphosis of Mg(SO$_3$CF$_3$)$_2$-based electrolytes for rechargeable magnesium batteries. *ChemElectroChem*, e202300664 (2024).

58. Bard, A. J., Faulkner, L. R. & White, H. S. Electrochemical methods: fundamentals and applications. *John Wiley & Sons.*, (2022).

59. Darling, R. M. Techno-economic analyses of several redox flow batteries using levelized cost of energy storage. *Curr. Opin. Chem. Eng.* **37**, 100855 (2022).

60. Li, Z., Fang, X., Cheng, L., Wei, X. & Zhang, L. Techno-economic analysis of non-aqueous hybrid redox flow batteries. *J. Power Sources* **536**, 231493 (2022).

61. Tang, L., *et al.* Capital cost evaluation of conventional and emerging redox flow batteries for grid storage applications. *Electrochim. Acta* **437**, 141460 (2023).

62. Minke, C. & Dorantes Ledesma, M. A. Impact of cell design and maintenance strategy on life cycle costs of vanadium redox flow batteries. *J. Energy Storage* **21**, 571–580 (2019).

63. https://www.sigmaaldrich.com/US/en/product/sigma/l090001 (Last accessed: April 2024).

64. https://www.sigmaaldrich.com/US/en/product/aldrich/746738 (Last accessed: April 2024).
65. https://www.sigmaaldrich.com/US/en/product/sigma/m8266 (Last accessed: April 2024).
66. https://www.sigmaaldrich.com/US/en/product/aldrich/281026 (Last accessed: April 2024).
67. https://www.sigmaaldrich.com/US/en/product/aldrich/544094 (Last accessed: April 2024).
68. https://www.sigmaaldrich.com/US/en/product/aldrich/214000 (Last accessed: April 2024).
69. https://www.sigmaaldrich.com/US/en/product/aldrich/221899 (Last accessed: April 2024).